Photoacoustics 34 (2023) 100569

Contents lists available at ScienceDirect

Photoacoustics

journal homepage: www.elsevier.com/locate/pacs

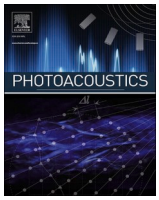

# *In vivo* liver function reserve assessments in alcoholic liver disease by scalable photoacoustic imaging

Tong Sun [b,c,1], Jing Lv [a,b,1], Xingyang Zhao [b], Wenya Li [b], Zhenhui Zhang [c], Liming Nie [b,*]

[a] Guangdong Cardiovascular Institute, Guangzhou 510080, China
[b] Medical Research Institute, Guangdong Provincial People's Hospital, Guangdong Academy of Medical Sciences, Southern Medical University, Guangzhou 510080, China
[c] MOE Key Laboratory of Laser Life Science & Institute of Laser Life Science, South China Normal University, Guangzhou 510631, China

ARTICLE INFO

*Keywords:*
Scalable photoacoustic imaging
Dynamic contrast enhancement
Alcoholic liver disease
Liver function reserve

ABSTRACT

We present a rapid and high-resolution photoacoustic imaging method for evaluating the liver function reserve (LFR). To validate its accuracy, we establish alcoholic liver disease (ALD) models and employ dual-wavelength spectral unmixing to assess oxygen metabolism. An empirical mathematical model fits the photoacoustic signals, obtaining liver metabolism curve and LFR parameters. Liver oxygen metabolism significantly drops in ALD with the emergence of abnormal hepatic lobular structure. ICG half-life remarkably extends from 241 to 568 s in ALD. A significant decline in LFR occurs in terminal region compared to central region, indicated by a 106.9 s delay in ICG half-life, likely due to hepatic artery and vein damage causing hypoxia and inadequate nutrition. Reduced glutathione repairs LFR with a 43% improvement by reducing alcohol-induced oxidative damage. Scalable photoacoustic imaging shows immense potential for assessing LFR in alcoholic-related diseases, providing assistance to early detection and management of liver disease.

## 1. Introduction

Alcoholic liver disease (ALD) is a prevalent and serious health issue worldwide, resulting from the excessive consumption of alcohol [1,2]. It poses a significant risk to individuals, leading to severe complications, ranging from steatosis to steatohepatitis [3], fibrosis [4], cirrhosis [5], and hepatocellular carcinoma [6]. Early detection and accurate assessment of ALD are crucial for effective management and improved patient outcomes.

In recent years, advancements in medical imaging techniques have opened new avenues for non-invasive assessment of liver diseases. Photoacoustic imaging (PAI) has emerged as a promising modality that combines the benefits of high-resolution imaging, deep tissue penetration [7,8], and functional information [9]. PAI utilizes laser-induced photoacoustic signals to generate detailed images by detecting the acoustic waves produced from the absorption of pulsed laser light by tissue chromophores [10,11]. PAI has demonstrated a variety of biological applications, such as detecting hemoglobin oxygen saturation ($sO_2$) [12,13], measuring blood flow velocity [14,15], enabling whole-body imaging in small animals [16], and facilitating preclinical cancer diagnosis [17–19].

PAI holds great promise in ALD assessment, particularly in evaluating hepatic vascular structure and oxygen metabolism [20,21], which are closely associated with liver function reserve (LFR) [16,22]. The vascular network is vital for liver health, providing the necessary nutrients and oxygen [23,24]. Disruption in vascular structure and oxygen metabolism indicate liver damage and impaired LFR [25]. LFR represents the metabolic capacity of liver and is a critical parameter for assessing disease severity and predicting patient outcomes [26]. Traditional static liver function tests and imaging modalities have limitations in comprehensive and real-time LFR evaluation. While hematological tests and clinical grading systems can identify liver lesions to some extent, they fall short in assessing LFR comprehensively [27,28].

Imaging techniques like computed tomography and magnetic resonance imaging lack quantitative evaluation and real-time monitoring of LFR changes [29,30].

The decline in indocyanine green (ICG) concentration reliably indicates liver function and is commonly employed in LFR assessment [10,31]. ICG clearance is calculated by collecting blood samples are 2–4 times within 15 min after intravenous ICG infusion and measuring their

* Corresponding author.
*E-mail address:* nieliming@gdph.org.cn (L. Nie).
[1] These authors contributed equally to this work.

https://doi.org/10.1016/j.pacs.2023.100569
Received 26 June 2023; Received in revised form 9 October 2023; Accepted 5 November 2023
Available online 7 November 2023

absorbance in vitro [28]. However, this process is invasive, inconvenient, and lacks real-time LFR results. Current ALD diagnosis methods, such as liver biopsy and imaging techniques, have drawbacks including invasiveness [32], sampling errors, low specificity [33], and resolution limitations [34]. Consequently, there is an urgent need for a comprehensive and precise technology to assess the metabolic function and vascular structure, highlighting the importance of LFR assessment.

We aim to enhance the ability to assess the LFR in ALD patients by leveraging the advantages of PAI. To validate the accuracy and sensitivity of PAI in assessing LFR, we established an ALD mouse model at different stages. The high-resolution advantage of PAI allowed to visualize vascular structure differences in the liver at varying health levels and located lesions. Dual-wavelength spectral unmixing was employed to evaluate liver hemoglobin oxygen saturation ($sO_2$), and an empirical mathematical model derived LFR-related parameters, including maximum peak time ($t_{max}$) and half-life ($t_{1/2}$). Statistical analysis of these parameters facilitates a comprehensive comparison of the pathological features between normal liver and ALD liver, further enabling the evaluation of metabolic capacity in different liver sub-regions.

In addition, reduced glutathione (GSH) is a potent antioxidant known for its important role in repairing liver function and alleviating alcohol-induced oxidative damage effects [6]. Combined GSH as a therapeutic intervention for ALD is expected to improve LFR and alleviate disease progression. PAI can potentially aid in monitoring the efficacy of GSH-based therapies by non-invasively assessing changes in the vascular structure and oxygen metabolism of the liver.

We offer an innovative method for the application of scalable PAI to the assessment of LFR in ALD, which is expected to unravel the intricate relationship between vascular abnormalities, oxygen metabolism and LFR, thereby enhancing the understanding of the pathogenesis of ALD (Fig. 1). Further research and clinical application of PAI in the treatment of ALD have the potential to revolutionize the diagnosis and treatment of liver disease, ultimately improving patient outcomes and quality of life.

## 2. Material and methods

### 2.1. Preparation of animals

All animals were obtained from the Guangdong Experimental Animal Center. The experimental protocols were approved by the ethics committee of Guangdong provincial people's hospital, and complied with all relevant ethical regulations. Male BALB/c-nude mice aged 6–8 weeks were housed in a 12-hour light/12-hour dark cycle with food and water. A total of 49 male mice were randomly divided into four groups: acute ALD (n = 14), chronic ALD (n = 7), GSH intervention (n = 7) and control (n = 21). Acute ALD group received alcohol (3 mg/kg body weight with 56% (v/v)) before imaging, while the chronic ALD group received 56% (v/v) alcohol (1 mg/kg body weight) daily for four weeks. The GSH group received 56% (v/v) alcohol (1 mg/kg body weight) intragastric administration, followed by an intravenous injection of reduced GSH 12 h later (5 mg/kg body weight), once a day for four weeks. The control group received a conventional diet.

### 2.2. PAM experiment

In the acute ALD mice liver structure imaging experiment, mice were anesthetized with 2% isoflurane. Abdominal incisions of 5 mm were made to expose the liver lobe. The functional information of the liver lobule was measured by dual wavelengths of 532 nm and 559 nm (high hemoglobin absorption), monitoring $sO_2$ changes within 30 min. Scanning parameters were set as follows: imaging range 2 mm × 2 mm, scanning step 5 μm, and laser frequency 1 kHz. For the chronic ALD and the GSH groups, the liver lobes were exposed surgically as described above. The wavelength of 532 nm was selected to obtain the structural information of the liver lobule.

### 2.3. PACT experiment

Each mouse remained under 2% isoflurane anesthesia throughout the experiment, with the body fixed upright in the center of the tank. In

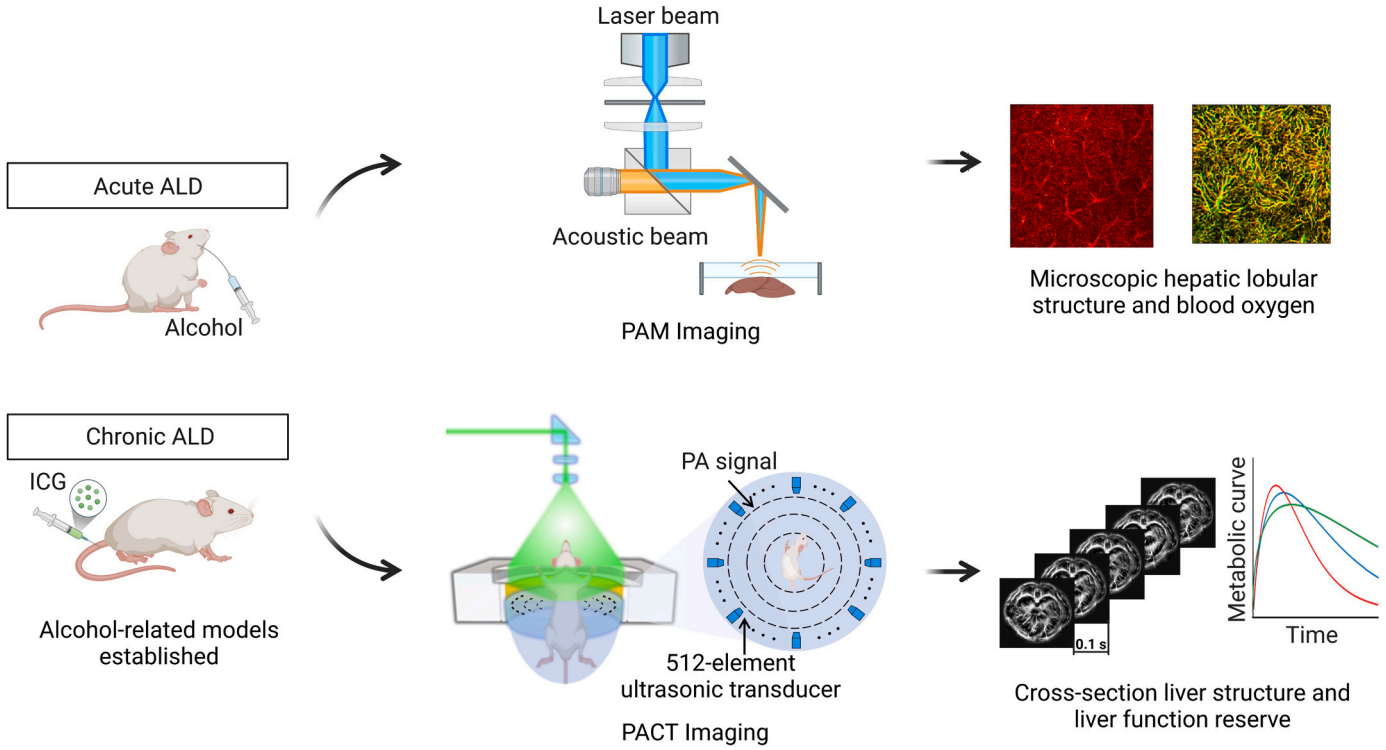


**Fig. 1.** Schematic diagram for establishment of alcoholic models and representative implementations of PAI.

the acute ALD group, images at wavelengths of 1064 nm and 780 nm were captured after alcohol administration to calculate sO2. In the chronic ALD and GSH groups, an indwelling needle was inserted into the mouse tail vein prior to imaging. An injection pump (D107886, KD Scientific Inc., USA) delivered 0.1 mL (3 mmol/kg body weight) of ICG solution at 0.2 mL/s. The laser wavelength was set at 780 nm, and a cross-section of mouse liver was scanned and imaged. Photoacoustic signals were continuously collected for 10 min. The control group was injected with the same volume of normal saline.

### 2.4. Photoacoustic imaging system

PAM (G2, InnoLaser) offers optical-to-acoustic resolution conversion with up to 5 μm optical resolution, supporting multi-wavelength laser scanning at 532 nm, 559 nm, and 750–840 nm. The acoustic signal generated by laser irradiation on the tissue was received by a 50 MHz ultrasonic sensor. The laser pulse repetition frequency is set to 10 kHz, and the X-axis B-scan rate is 25 Hz.

PACT (SIP-PACT, Union Photoacoustic Technologies) can be used for organs cross-section imaging. It is equipped with a laser with a 20 Hz repetition rate, enabling imaging at wavelengths of 680–950 nm, 1064 nm, and 1190–2600 nm. A 512-element ring array ultrasonic transducer with a center frequency of 5.5 MHz is used to collect ultrasonic signals. The imaging resolution is 125 μm, and the imaging depth is approximately 5 cm.

### 2.5. Signal and image processing

MATLAB 9.8 software (R2020a, MathWorks) was used for image processing. Raw data was reconstructed by the dual acoustic back-projection algorithm to generate a PA image. Vascular features were extract from the PA images using the Hessian Filter Enhancement algorithm, providing more detailed information. The differential image was obtained by subtracting the baseline image from the post-injection. The portion of the image whose signal value was greater than the average pixel was chosen as the enhancement part and assigned color pixels. It was then overlaid on a 1064 nm background image.

To image the mouse liver, two different wavelengths of laser pulses (1064 nm and 780 nm) were used. The 1064 nm wavelength provides deep penetration, enabling clearer image of the liver structure. In the range of 600–800 nm, oxygenated hemoglobin ($HbO_2$) and deoxygenated hemoglobin (Hb) have distinct absorption coefficients. The wavelength of 780 nm can achieve high contrast to distinguish the signals of oxyhemoglobin and deoxyhemoglobin. Photoacoustic images at 1064 nm and 780 nm were used for spectral unmixing to calculate $sO_2$ [35].

Binary conversion was applied to transform photoacoustic images into binary images represented by single-bit pixels (0 or 1). Intensity-based thresholding (0.3) was employed to identify and extract regions of interest. Abnormal blood vessels were recognized using a clustering algorithm based on vessel diameter characteristics [36].

### 2.6. Empirical mathematical model

Origin 2016 was used for all data processing. The base value for monitoring liver ICG metabolism was obtained by averaging 300 image signal values before ICG injection. The image signal value was quantified within 10 min of ICG injection, and the metabolic curve was drawn after filtering and smoothing. Relative intensity ($R_I$) of the ICG signal was calculated using the following formula [37]:

$$R_I = [PA(t) - PA(0)]/[PA(0)] \quad (1)$$

where *PA(t)* represents post-injection time-varying photoacoustic signal value, and *PA(0)* is the pre-injection basis value. The metabolic curve can be fitted according to the following formula [38]:

$$R_I = \begin{cases} 0, 0 \le t < t_0 \\ A\cdot\left[1 - e^{-\alpha(t-t_0)}\right]\cdot q\cdot e^{\beta(t-t_0)}, t_0 \le t \end{cases} \quad (2)$$

where $A$ is the maximum amplitude of $R_I$, t is the time variable (s), $\alpha$ is the rate of drug uptake ($s^{-1}$), $\beta$ is the rate of drug metabolism ($s^{-1}$), and $q$ is the parameter associated with the slope of early uptake. Maximum peak time ($t_{max}$) of $R_I$ and half-life of metabolism ($t_{1/2}$) were derived from the fitted curves.

### 2.7. Statistical analysis

SPSS27 software (IBM, USA) was utilized for the statistical analysis. One-way ANOVA was used to compare the results between groups after checking the normality of $sO_2$ data. A two-tailed P value less than 0.05 was indicative of a significant difference. Quantitative data of hepatic metabolic parameters were displayed as mean ± standard deviation.

### 2.8. Histopathology of liver

After paraffin embedding, the liver tissue was fixed with a 10% paraformaldehyde solution and sectioned. The tissue slices were stained by hematoxylin and eosin. Frozen liver slices were dried and incubated in 100% isopropanol before being stained with oil red O. Histopathological changes in the liver were examined under a microscope.

## 3. Results

### 3.1. Blood oxygen levels in mice with acute ALD

PAM and PACT monitored $sO_2$ changes in the livers of mice after acute alcohol administration at multi-scale. PAM images (Fig. 2a) displayed the microstructure and function of the hepatic lobules, which are the primary liver unit. Alcohol gavage had no significant impact on the microstructure of hepatic lobules, but $sO_2$ steadily declined (Before: 84.3 ± 2.1%, 30 min: 71.5 ± 5.0%, $p < 0.05$). In the control group, $sO_2$ initially dropped and then increased (Before: 84.79 ± 2.86%, 30 min: 83.0 ± 2.4%, $p < 0.05$). Fig. 2b depicted the entire liver cross-section by PACT. In the acute ALD group, sO2 gradually decreased within 30 min after alcohol gavage (Before: 91.8 ± 5.0%, 30 min: 52.1 ± 3.4%, $p < 0.01$). In the control group, $sO_2$ decreased slightly after 5 min of saline injection, then returned to normal (Before: 84.9 ± 0.2%, 30 min: 83.8 ± 1.4%, $p < 0.01$), consistent with PAM results.

### 3.2. Evaluating the LFR in chronic ALD mice by PACT

PACT enabled macroscopic liver imaging, visualizing the vascular network and hepatic cross-section tissues. Dynamic recordings captured vibrations of the portal vein, inferior vena cava, and abdominal aorta. ICG is an FDA-approved contrast agent, served as an optical indicator for clinical liver function testing. Fig. 3(a)–(c) illustrated the photoacoustic signals from liver slices recorded within 600 s after ICG injection for LFR assessment. The color signal indicated time-dependent ICG uptake in the liver. LFR curves for the three liver groups were shown in Fig. 3(d)–(f). Long-term alcohol consumption negatively affects liver blood vessels, further impairing liver function. Fig. 3(g) displayed prolonged $t_{max}$ of ICG in the chronic ALD group compared to the control, while it was shorter following GSH administration (Control: 91.9 ± 3.0 s, Chronic ALD: 139.8 ± 12.4 s, GSH: 120.8 ± 13.4 s, $p < 0.05$). The rate of ICG clearance in the chronic ALD group was approximately twice as slow as the control group. Compared to the control group, the $t_{1/2}$ in the GSH group was a slightly longer (Control: 241.0 ± 8.0 s, Chronic ALD: 568.2 ± 23.2 s, GSH: 356.1 ± 10.8 s, $p < 0.01$). These findings indicate that alcohol impaired liver LFR. GSH effectively repaired LFR ($t_{1/2}$) with ~43% improvement by reducing alcohol-induced oxidative damage. Interestingly, early intervention alleviated the negative effects of

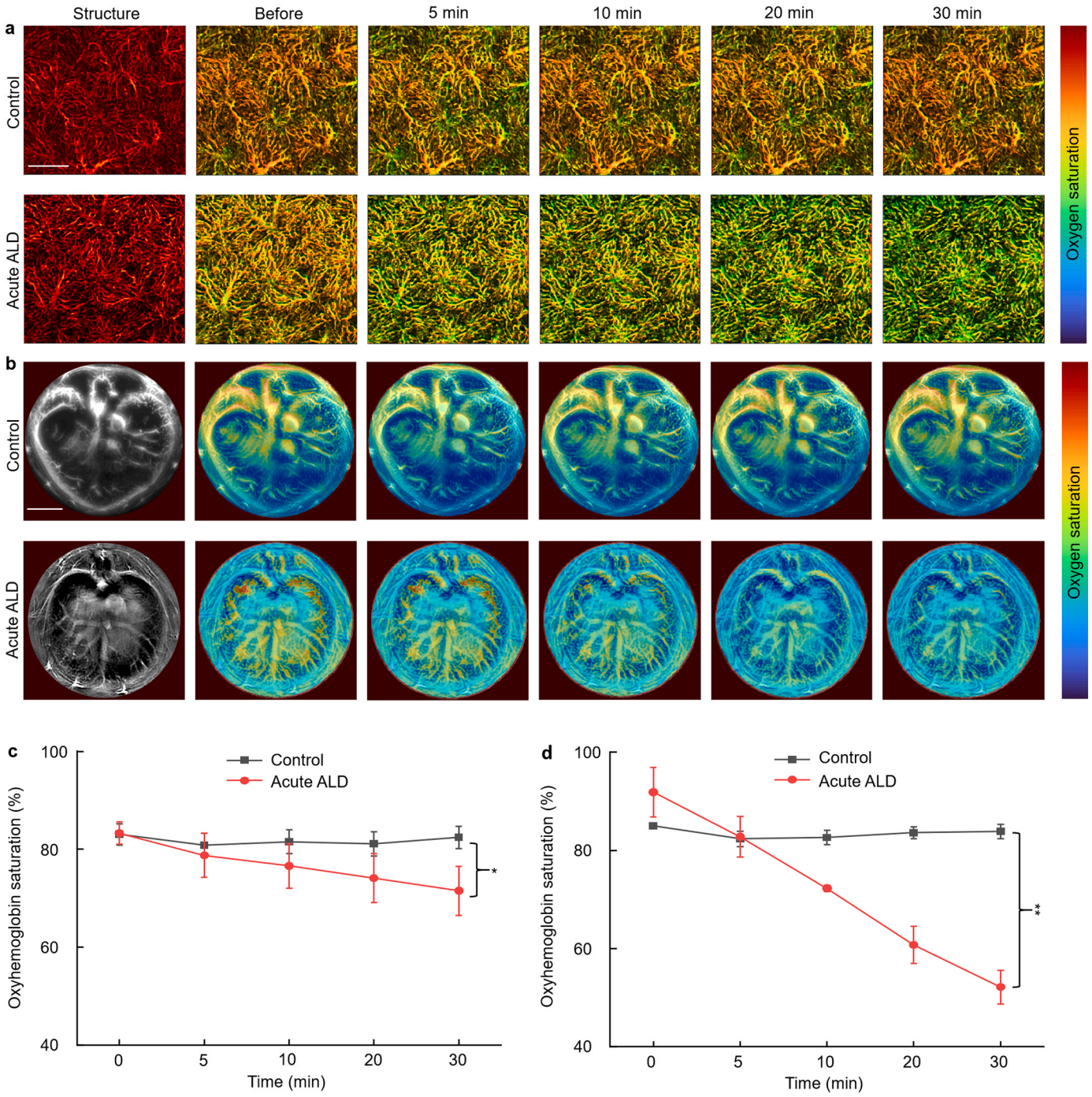


**Fig. 2.** Microstructural and oxygen metabolism imaging of the liver in acute ALD model. (a) PAM was used to monitor $sO_2$ images in the liver within 30 min in control and acute ALD groups. (b) PACT was used to monitor $sO_2$ images in the liver within 30 min in control and acute ALD groups. Quantitative oximetry data from (c) PAM and (d) PACT. Scale bars: 500 μm (PAM), 5 mm (PACT). *, $p < 0.05$, **, $p < 0.01$.

alcohol on liver function.

### 3.3. Changes in LFR based on different liver sub-areas

Drug metabolism is a crucial liver function for eliminating foreign substances such as drugs, alcohol, and poisons. It was found that ICG was metabolized differently in the various areas of the whole liver. The results showed that $t_{1/2}$ in the central region (yellow dashed box, Fig. 4 (b)) was 208.5 ± 9.0 s, and 220.3 ± 8.9 s in the terminal region (red dashed box, Fig. 4(c)) in the control group. In the chronic ALD group, $t_{1/2}$ in the central region (yellow dashed box, Fig. 4(e)) was 500.6 ± 21.4 s, and it was 619.3 ± 18.3 s in the terminal region (red dashed box, Fig. 4 (f)). Analysis revealed a ~400 s prolongation of $t_{1/2}$ in the terminal region and ~300 s in the central region in the chronic ALD group compared to the control. Long-term alcohol use affected liver metabolism more severely in the terminal region than in the central region. It is speculated that chronic ALD leads to hepatocyte necrosis, causing a disruption in the continuity of hepatic vascular structure. Moreover, the functions of the portal vein (providing nutrients) and hepatic artery (providing oxygen) were impaired. Fig. 4(a) and (d) depicted insufficient nourishment and oxygen in the tissues of the terminal liver region compared to the central region. Hence, the damage was more severe,

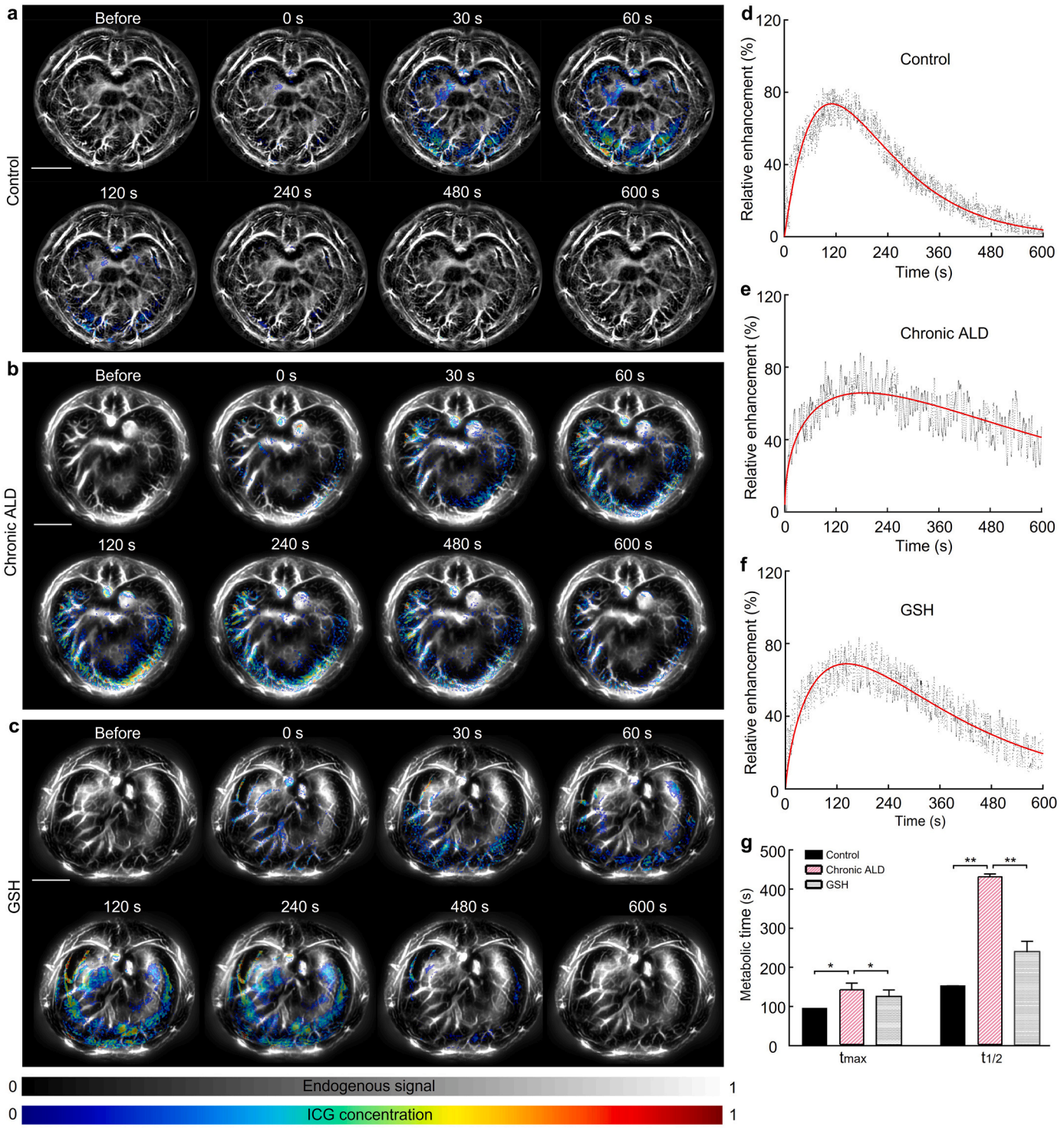


**Fig. 3.** Time course of LFR in mice liver was measured by PACT. PACT images visualizing ICG clearance in (a) control, (b) chronic ALD, and (c) GSH groups. (d), (e), and (f) Liver metabolic curves in different groups. (g) Quantitative data of kinetic parameters $t_{max}$ and $t_{1/2}$. All scale bars are 5 mm. *, $p < 0.05$, **, $p < 0.01$.

resulting in a significant decline in LFR.

### 3.4. Microscopic imaging of liver structures in chronic ALD mice

To examine micro-level structural abnormalities in the livers of chronic ALD mice, PAM scans were conducted. Fig. 5(a) revealed distinct liver lobule structure and well-organized blood vessels in healthy mice. In the chronic ALD group, blood vessels appeared blurry with numerous vascular nodules. Furthermore, liver lobes presented partial edema and fatty lesions. The GSH group showed mild vessel swelling and a few vascular nodules, primarily due to local inflammation caused by alcohol abuse. Fig. 5(b) binarized the microscopic images to highlight vascular continuity. The chronic ALD group showed a wide range of vascular signal loss, indicating a higher prevalence of steatosis around vessels. In comparison, the GSH group exhibited less damage. Fig. 5(c) utilized a vascular feature algorithm to identify the abnormal vascular region in red. The chronic ALD group displayed the largest abnormal vascular area.

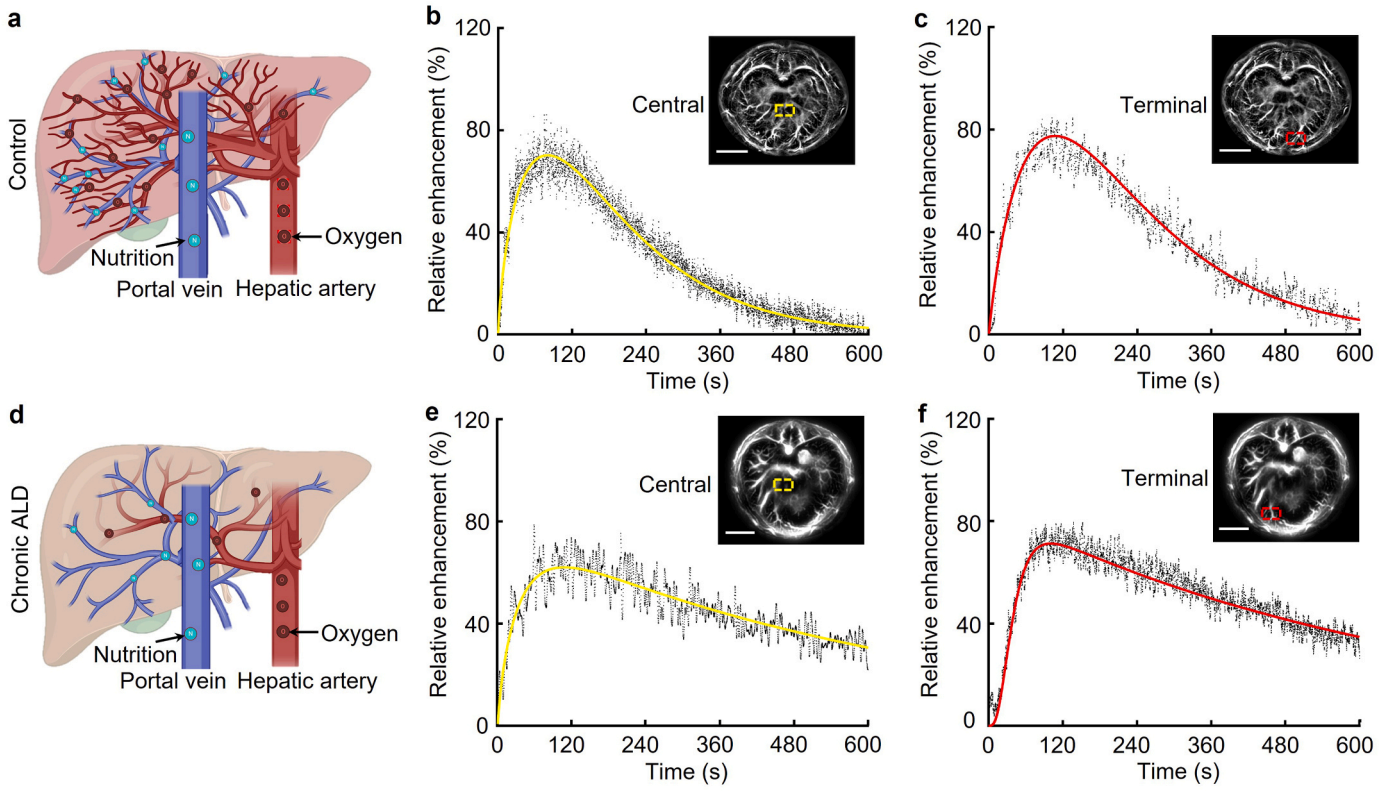


**Fig. 4.** Time course of LFR in mice liver sub-areas. Blood vessels transporting nutrients and oxygen in the liver in (a) control and (d) chronic ALD groups. Metabolic curves of the central region in (b) control and (c) chronic ALD groups. Metabolic curves of the terminal region in (e) control and (f) chronic ALD groups. All scale bars are 5 mm.

### *3.5. Pathophysiological examination*

The pathogenic structure of chronic ALD was showed in Fig. 6(a), highlighting noticeable pathological abnormalities compared to the control group. These abnormalities included disorganized hepatic cords, irregularly arranged hepatic plates, neutrophil infiltration, hepatocyte vacuolation, mallory body presence, and steatosis (shown in I and II in the second row). Similarly, Fig. 6(b) showed a more severe fatty liver in the chronic ALD group.

The changes in serum alanine transaminase (ALT), aspartate transaminase (AST), triglyceride (TG), and glutathione peroxidase (GSH-PX) can reflect the degree of ethanol-induced liver injury, as shown in Fig. 6 (c). The ALT, AST, and TG levels in the chronic ALD group were 110%, 163%, and 73% higher than the control, whereas GSH-PX was 20% lower. After GSH intervention, serum ALT and AST levels in chronic ALD mice decreased to some extent. Acetaldehyde dehydrogenase (ADH) and alcohol dehydrogenase (ALDH) are key enzymes in ethanol metabolism. Compared to the control group, the ADH activity in chronic ALD group was noticeably reduced, although it increased after GSH intervention, as shown in Fig. 6(c). Liver ALDH activity in both the chronic ALD and GSH groups increased by 43% and 118%, respectively. These results indicated that the liver of chronically alcohol-consuming mice could better metabolize alcohol with the help of GSH.

## 4. Discussion

In this study, dynamic PAI was utilized to demonstrate the microscopic and macroscopic features of the early stages of ALD. Traditional ALD diagnostic methods, such as liver biopsy and various imaging techniques, suffer from invasiveness, sampling errors, low specificity, and limited resolution. Therefore, we combined PAM and PACT to provide a more comprehensive perspective for ALD research. Alcohol consumption altered liver vascular structure and functional parameters, including oxygen metabolism, demonstrated through PAM and PACT. Quantitative analysis of the light absorption intensity of $HbO_2$ and Hb at different wavelengths allows accurate assessment the $sO_2$ levels. Excessive alcohol intake rapidly decreases the $sO_2$ levels in the liver, causing acute hypoxia and potential liver failure. Studies suggest alcohol hinders the absorption of oxygen by hemoglobin, causing red blood cell agglutination and impaired organ oxygen delivery [39].

ICG concentration decline is widely used to reflect liver function. However, ICG clearance rate testing is invasive and not real-time. We present a non-invasive method based on rapid and dynamic PACT for accurate LFR assessment. Understanding liver metabolism is crucial for optimal medication therapy. ICG is a key dye for monitoring LFR and hemodynamics. Combining ICG with photoacoustic technology enables us to evaluate the severity of liver disease by measuring dye metabolism and clearance rate of the. We quantified the time course curve of ICG by measuring photoacoustic signal intensity changes. Results showed significant metabolic differences between healthy and sick livers, with prolonged $t_{max}$ and $t_{1/2}$ of ICG observed after alcohol injury. GSH intervention partially recovers liver metabolic capacity and reduces vascular steatosis severity. This non-invasive method, with fast, multi-wavelength, wide-field, and high-resolution capabilities, provides a new strategy for clinical LFR evaluation.

Alcohol primarily damages the liver terminal region, impacting the nutrients and oxygen transport during ALD [35]. The integrity and functionality of the liver blood vessels are also damaged. Moreover, since the terminal region is far from the center, these factors lead to insufficient nutrient supply (portal vein) and oxygen supply (hepatic artery) to the terminal region. PAI can zone the LFR by accurately evaluating the metabolic capacity of different sub-areas.

The liver converts alcohol into water and carbon dioxide [3,23]. Prolonged alcohol consumption alters enzyme activity. According to

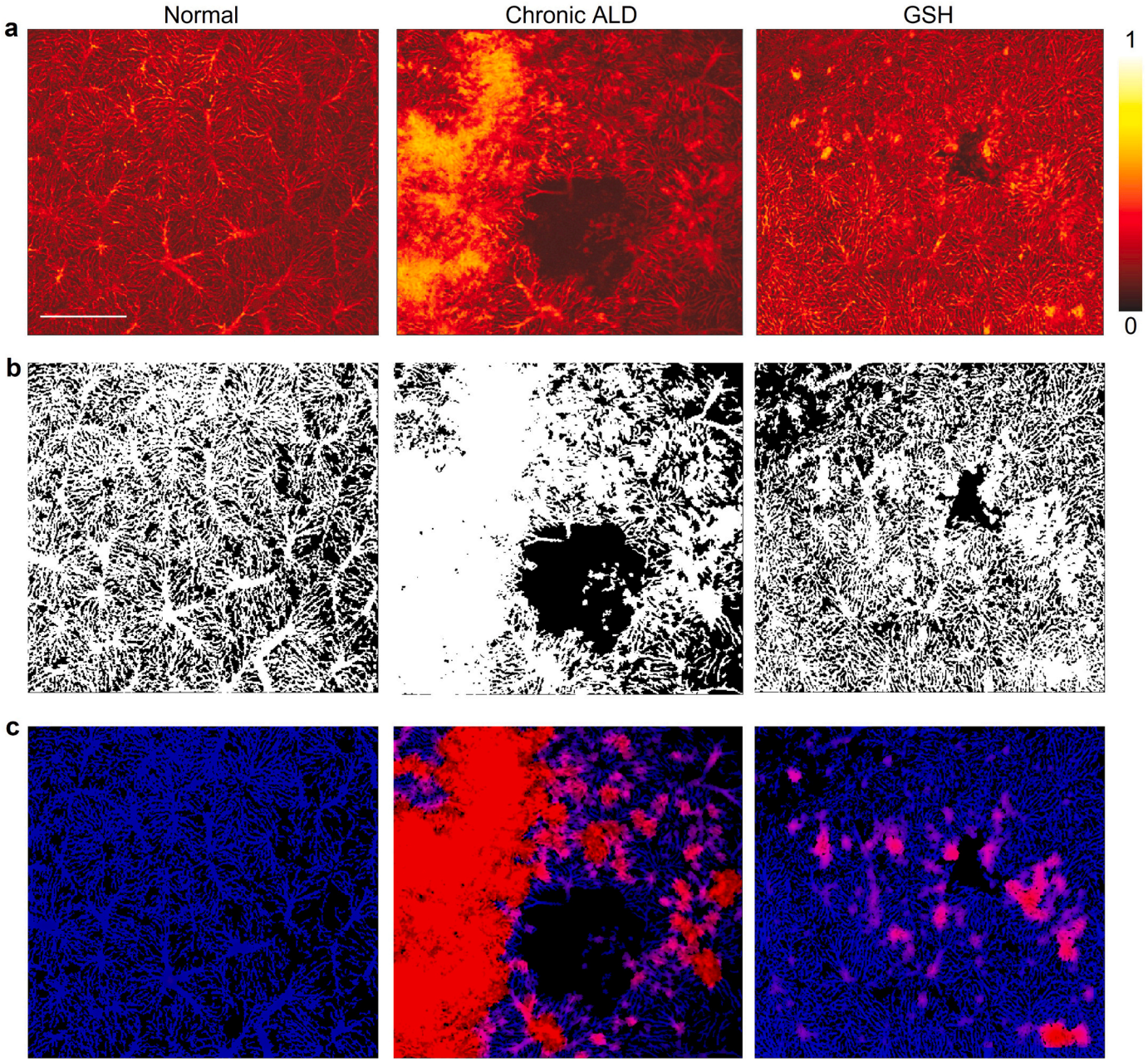


**Fig. 5.** Structural images of the liver were obtained by PAM at 532 nm. (a) Photoacoustic images. (b) The image after filtering and binarization of figure (a). (c) Abnormal blood vessel images by feature extraction. All scale bars are 500 μm.

studies, ethanol exposure generates free radicals and oxidants, increasing GSH utilization for detoxification [40]. GSH is crucial in mitigating alcohol-induced oxidative damage.

This study utilizes two imaging technologies: Photoacoustic microscopy excels in high-resolution imaging, revealing microvascular morphology and providing vital tissue functionality information, including oxygen saturation. Additionally, its precise localization capabilities enhance accuracy and visual effectiveness in detecting anomalous blood vessels. On the other hand, photoacoustic computed tomography demonstrates real-time dynamic visualizations of the liver noninvasively. It offers a powerful tool for diagnosing and monitoring liver diseases with broad clinical applications. By harnessing the synergies of these two imaging systems, this study maximizes the unique advantages of photoacoustic technology in liver research and medical applications.

In summary, recent advancements in PAI hold promise for assessing ALD by visualizing and quantifying liver vascular structure, oxygen saturation, and LFR. This non-invasive technique has significant clinical applications in ALD diagnosis and management. Ongoing research in PAI techniques have the potential to revolutionize ALD assessment, leading to improved patient outcomes.

## 5. Conclusion

We introduced an innovative multi-scale PAI technique for precise measurement of LFR. Compared to traditional clinical imaging, PAI offers non-invasiveness and high-contrast visualization, potentially enhancing comprehensive assessment of hepatic diseases. However, challenges in imaging speed arise due to limitations in laser frequency and B-scan rates. PAM primarily targets surface microvasculature, yet deep vascular lesions are crucial for hepatic disease diagnosis. Our next step improvements involve enhancing imaging speed and depth while

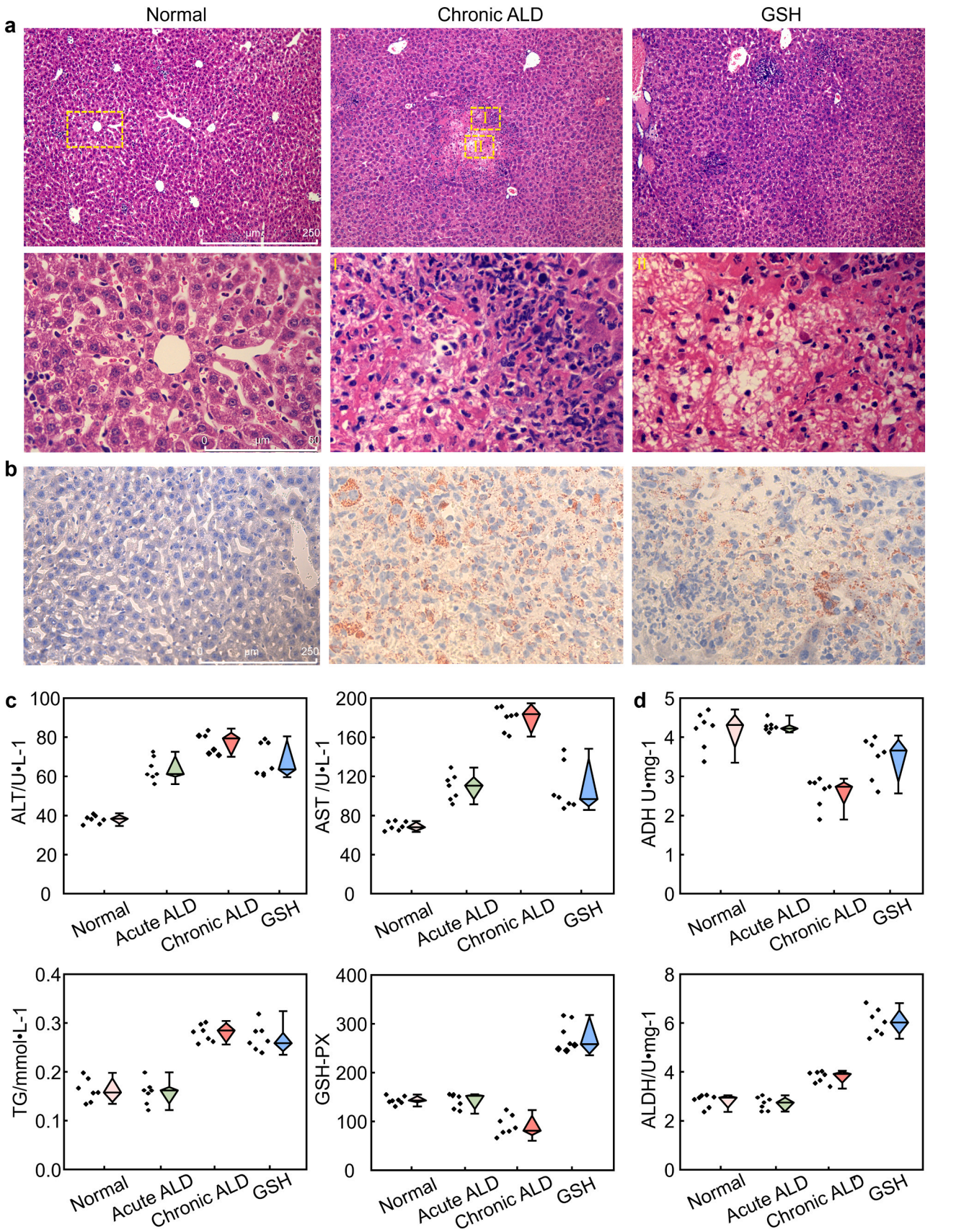


**Fig. 6.** Pathological sections of mouse livers from three groups were stained with hematoxylin and eosin. (a) The sections were magnified at × 100 and × 400 in Row 1 and Row 2, respectively. The second row is an enlarged image of the area enclosed by the yellow box from the first row. (b) The oil-red O section was magnified at × 400. (c) Blood biochemical index. (d) Enzyme activity.

maintaining system stability through higher laser frequencies, and optimized scanning algorithms.

In summary, our research provides opportunities for hepatic disease diagnosis and monitoring. We anticipate wide interest across research domains, advancing medical imaging and disease diagnosis research.

## Funding

This investigation was supported by grants from National Natural Science Foundation of China (82372010&82302253) and GDPH Supporting Fund for Talent Program (KJ01200638).

## Declaration of Competing Interest

The authors declare that there are no conflicts of interest.

## Data availability

For inquiries regarding the availability of the code, you are welcome to contact after the article publication, due to intellectual property considerations.

## Acknowledgments

T. Sun and J. Lv contributed equally to this work. All authors contributed to the study conception and design. All authors read and approved the final manuscript.

## References

[1] L. Vonghia, L. Leggio, A. Ferrulli, M. Bertini, G. Gasbarrini, G. Addolorato, G. Alcoholism Treatment Study, Acute alcohol intoxication, Eur. J. Intern. Med. 19 (8) (2008) 561–567, https://doi.org/10.1016/j.ejim.2007.06.033.

[2] G.B.D.A. Collaborators, Alcohol use and burden for 195 countries and territories, 1990-2016: a systematic analysis for the Global Burden of Disease Study 2016, Lancet 392 (10152) (2018) 1015–1035, https://doi.org/10.1016/S0140-6736(18)31310-2.

[3] M.R. Lucey, P. Mathurin, T.R. Morgan, Alcoholic hepatitis, N. Engl. J. Med. 360 (26) (2009) 2758–2769, https://doi.org/10.1056/NEJMra0805786.

[4] M.R. Thursz, P. Richardson, M. Allison, A. Austin, M. Bowers, C.P. Day, N. Downs, D. Gleeson, A. MacGilchrist, A. Grant, S. Hood, S. Masson, A. McCune, J. Mellor, J. O'Grady, D. Patch, I. Ratcliffe, P. Roderick, L. Stanton, N. Vergis, M. Wright, S. Ryder, E.H. Forrest, S. Trial, Prednisolone or pentoxifylline for alcoholic hepatitis, N. Engl. J. Med. 372 (17) (2015) 1619–1628, https://doi.org/10.1056/NEJMoa1412278.

[5] R.E. Childers, J. Ahn, Diagnosis of alcoholic liver disease: key foundations and new developments, Clin. Liver Dis. 20 (3) (2016) 457–471, https://doi.org/10.1016/j.cld.2016.02.005.

[6] N.A. Osna, T.M. Donohue Jr., K.K. Kharbanda, Alcoholic liver disease: pathogenesis and current management, Alcohol Res. 38 (2) (2017) 147–161.

[7] H. Ma, Z. Cheng, Z. Wang, H. Qiu, T. Shen, D. Xing, Y. Gu, S. Yang, Quantitative and anatomical imaging of dermal angiopathy by noninvasive photoacoustic microscopic biopsy, Biomed. Opt. Express 12 (10) (2021) 6300–6316, https://doi.org/10.1364/BOE.439625.

[8] D. Zhang, Z. Wang, Z. Cheng, W. Zhang, F. Yang, S. Yang, An ellipsoidal focused ultrasound transducer for extend-focus photoacoustic microscopy, IEEE Trans. Biomed. Eng. 68 (12) (2021) 3748–3752, https://doi.org/10.1109/TBME.2021.3078729.

[9] S. Richard, A.E. Sergey, L. Anton, A.O. Alexander, Three-dimensional optoacoustic imaging as a new noninvasive technique to study long-term biodistribution of optical contrast agents in small animal models, J. Biomed. Opt. 17 (10) (2012), 101506, https://doi.org/10.1117/1.JBO.17.10.101506.

[10] L.V. Wang, Multiscale photoacoustic microscopy and computed tomography, Nat. Photonics 3 (9) (2009) 503–509, https://doi.org/10.1038/nphoton.2009.157.

[11] H. He, C. Schonmann, M. Schwarz, B. Hindelang, A. Berezhnoi, S.A. Steimle-Grauer, U. Darsow, J. Aguirre, V. Ntziachristos, Fast raster-scan optoacoustic mesoscopy enables assessment of human melanoma microvasculature in vivo, Nat. Commun. 13 (1) (2022) 2803, https://doi.org/10.1038/s41467-022-30471-9.

[12] Z. Jason, M.R. Lisa, A.C. Bryan, H. Jeff, L.G.M. Gisela, A. Carlos, B. Allison, S. Xavier, C. Edgar, M. Steve, A.O. Alexander, C.K. Michael, Characterization of optoacoustic color mapping for oxygen saturation of blood using biologically relevant phantoms, Proc. SPIE, 2019, p. 108781Q. http://doi.org/10.1117/12.2506906.

[13] M.M. Menger, C. Körbel, D. Bauer, M. Bleimehl, A.L. Tobias, B.J. Braun, S. C. Herath, M.F. Rollmann, M.W. Laschke, M.D. Menger, T. Histing, Photoacoustic imaging for the study of oxygen saturation and total hemoglobin in bone healing and non-union formation, Photoacoustics 28 (2022), 100409, https://doi.org/10.1016/j.pacs.2022.100409.

[14] Q. Zhou, Z. Chen, Y.-H. Liu, M. El Amki, C. Glück, J. Droux, M. Reiss, B. Weber, S. Wegener, D. Razansky, Three-dimensional wide-field fluorescence microscopy for transcranial mapping of cortical microcirculation, Nat. Commun. 13 (1) (2022) 7969, https://doi.org/10.1038/s41467-022-35733-0.

[15] X.L. Deán-Ben, J. Robin, D. Nozdriukhin, R. Ni, J. Zhao, C. Glück, J. Droux, J. Sendón-Lago, Z. Chen, Q. Zhou, B. Weber, S. Wegener, A. Vidal, M. Arand, M. El Amki, D. Razansky, Deep optoacoustic localization microangiography of ischemic stroke in mice, Nat. Commun. 14 (1) (2023) 3584, https://doi.org/10.1038/s41467-023-39069-1.

[16] L. Li, L. Zhu, C. Ma, L. Lin, J. Yao, L. Wang, K. Maslov, R. Zhang, W. Chen, J. Shi, L. V. Wang, Single-impulse panoramic photoacoustic computed tomography of small-animal whole-body dynamics at high spatiotemporal resolution, Nat. Biomed. Eng. 1 (5) (2017) 0071, https://doi.org/10.1038/s41551-017-0071.

[17] Y. Qian, H. Shanshan, W. Zhiyou, Z. Jiadi, C. Xiaoyuan, N. Liming, Label-free visualization of early cancer hepatic micrometastasis and intraoperative image-guided surgery by photoacoustic imaging, J. Nucl. Med. 61 (7) (2020) 1079, https://doi.org/10.2967/jnumed.119.233155.

[18] N. Naoki, SvdB. Nynke, A.M. Brock, K. Stan van, F. Shayan, L.R. Eben, E. W. Katheryne, Photoacoustic molecular imaging for the identification of lymph node metastasis in head and neck cancer using an anti-EGFR antibody–dye conjugate, J. Nucl. Med. 62 (5) (2021) 648, https://doi.org/10.2967/jnumed.120.245241.

[19] Z. Wang, F. Yang, W. Zhang, K. Xiong, S. Yang, Towards in vivo photoacoustic human imaging: Shining a new light on clinical diagnostics, Fundam. Res. (2023), https://doi.org/10.1016/j.fmre.2023.01.008.

[20] Q. Wang, Y. Shi, F. Yang, S. Yang, Quantitative photoacoustic elasticity and viscosity imaging for cirrhosis detection, Appl. Phys. Lett. 112 (21) (2018), 211902, https://doi.org/10.1063/1.5021675.

[21] B. Lafci, A. Hadjihambi, C. Konstantinou, J.L. Herraiz, L. Pellerin, N.C. Burton, X. L. Deán-Ben, D. Razansky, Multimodal assessment of non-alcoholic fatty liver disease with transmission-reflection optoacoustic ultrasound, 2022.08.16.504139, bioRxiv (2022), https://doi.org/10.1101/2022.08.16.504139.

[22] J. Lv, Y. Xu, L. Xu, L. Nie, Quantitative functional evaluation of liver fibrosis in mice with dynamic contrast-enhanced photoacoustic imaging, Radiology 300 (1) (2021) 89–97, https://doi.org/10.1148/radiol.2021204134.

[23] H.K. Seitz, R. Bataller, H. Cortez-Pinto, B. Gao, A. Gual, C. Lackner, P. Mathurin, S. Mueller, G. Szabo, H. Tsukamoto, Alcoholic liver disease, Nat. Rev. Dis. Prim. 4 (1) (2018) 16, https://doi.org/10.1038/s41572-018-0014-7.

[24] K.M. Mak, C.Y.M. Png, The hepatic central vein: structure, fibrosis, and role in liver biology, Anat. Rec. 303 (7) (2020) 1747–1767, https://doi.org/10.1002/ar.24273.

[25] J. Gracia-Sancho, E. Caparros, A. Fernandez-Iglesias, R. Frances, Role of liver sinusoidal endothelial cells in liver diseases, Nat. Rev. Gastroenterol. Hepatol. 18 (6) (2021) 411–431, https://doi.org/10.1038/s41575-020-00411-3.

[26] D. D'Avola, A. Granito, Mdl Torre-Aláez, F. Piscaglia, The importance of liver functional reserve in the non-surgical treatment of hepatocellular carcinoma, J. Hepatol. 76 (5) (2022) 1185–1198, https://doi.org/10.1016/j.jhep.2021.11.013.

[27] F. Durand, D. Valla, Assessment of the prognosis of cirrhosis: Child-Pugh versus MELD, J. Hepatol. 42 (Suppl. 1) (2005) S100–S107, https://doi.org/10.1016/j.jhep.2004.11.015.

[28] J.J. Vos, J.G. Wietasch, A.R. Absalom, H.G. Hendriks, T.W. Scheeren, Green light for liver function monitoring using indocyanine green? An overview of current clinical applications, Anaesthesia 69 (12) (2014) 1364–1376.

[29] M. Nakagawa, T. Namimoto, K. Shimizu, K. Morita, F. Sakamoto, S. Oda, T. Nakaura, D. Utsunomiya, S. Shiraishi, Y. Yamashita, Measuring hepatic functional reserve using T1 mapping of Gd-EOB-DTPA enhanced 3T MR imaging: a preliminary study comparing with (99m)Tc GSA scintigraphy and signal intensity based parameters, Eur. J. Radiol. 92 (2017) 116–123, https://doi.org/10.1016/j.ejrad.2017.05.011.

[30] Y. Mizutani, T. Hirai, S. Nagamachi, A. Nanashima, K. Yano, K. Kondo, M. Hiyoshi, N. Imamura, T. Terada, Prediction of posthepatectomy liver failure proposed by the international study group of liver surgery: residual liver function estimation with 99mTc-galactosyl human serum albumin scintigraphy, Clin. Nucl. Med. 43 (2) (2018).

[31] G. Huang, J. Lv, Y. He, J. Yang, L. Zeng, L. Nie, In vivo quantitative photoacoustic evaluation of the liver and kidney pathology in tyrosinemia, Photoacoustics 28 (2022), 100410, https://doi.org/10.1016/j.pacs.2022.100410.

[32] K. Saito, J. Ledsam, S. Sourbron, T. Hashimoto, Y. Araki, S. Akata, K. Tokuuye, Measuring hepatic functional reserve using low temporal resolution Gd-EOB-DTPA dynamic contrast-enhanced MRI: a preliminary study comparing galactosyl human serum albumin scintigraphy with indocyanine green retention, Eur. Radiol. 24 (1) (2014) 112–119, https://doi.org/10.1007/s00330-013-2983-y.

[33] R.M.S. Sigrist, J. Liau, A.E. Kaffas, M.C. Chammas, J.K. Willmann, Ultrasound elastography: review of techniques and clinical applications, Theranostics 7 (5) (2017) 1303–1329, https://doi.org/10.7150/thno.18650.

[34] M.A. Avila, J.F. Dufour, A.L. Gerbes, F. Zoulim, R. Bataller, P. Burra, H. Cortez-Pinto, B. Gao, I. Gilmore, P. Mathurin, C. Moreno, V. Poznyak, B. Schnabl, G. Szabo, M. Thiele, M.R. Thursz, Recent advances in alcohol-related liver disease (ALD): summary of a Gut round table meeting, Gut 69 (4) (2020) 764–780, https://doi.org/10.1136/gutjnl-2019-319720.

[35] H. Roman, A. Lu, C.B. Paul, T.C. Benjamin, Estimating blood oxygenation from photoacoustic images: can a simple linear spectroscopic inversion ever work? J. Biomed. Opt. 24 (12) (2019), 121914 https://doi.org/10.1117/1.JBO.24.12.121914.

[36] S.A. Salem, N.M. Salem, A.K. Nandi, Segmentation of retinal blood vessels using a novel clustering algorithm (RACAL) with a partial supervision strategy, Med. Biol.

Eng. Comput. 45 (3) (2007) 261–273, https://doi.org/10.1007/s11517-006-0141-2.
[37] S. Saito, Y. Moriyama, S. Kobayashi, R. Ogihara, D. Koto, A. Kitamura, T. Matsushita, M. Nishiura, K. Murase, Assessment of liver function in thioacetamide-induced rat acute liver injury using an empirical mathematical model and dynamic contrast-enhanced MRI with Gd-EOB-DTPA, J. Magn. Reson. Imaging 36 (6) (2012) 1483–1489, https://doi.org/10.1002/jmri.23726.
[38] A. Oto, X. Fan, D. Mustafi, S.A. Jansen, G.S. Karczmar, D.T. Rubin, A. Kayhan, Quantitative analysis of dynamic contrast enhanced MRI for assessment of bowel inflammation in Crohn's disease: pilot study, Acad. Radiol. 16 (10) (2009) 1223–1230, https://doi.org/10.1016/j.acra.2009.04.010.
[39] H.S. Ballard, The hematological complications of alcoholism, Alcohol Health Res. World 21 (1) (1997) 42–52.
[40] A. Louvet, P. Mathurin, Alcoholic liver disease: mechanisms of injury and targeted treatment, Nat. Rev. Gastroenterol. Hepatol. 12 (4) (2015) 231–242, https://doi.org/10.1038/nrgastro.2015.35.

**Tong Sun** is a master's student at South China Normal University. Her research interests are in the development of photoacoustic imaging systems for medical applications.

**Jing Lv** is currently a postdoctoral fellow of Research Center of Medical Sciences of Guangdong Provincial People's Hospital, Guangdong Academy of Medical Sciences. She got his Ph.D. degree from Xiamen University, China in 2022. Her main research interests are the structural and functional photoacoustic imaging application of cardiovascular and cerebrovascular disease models as well as contrast-enhanced quantitative, dynamic, metabolic imaging of livers and kidneys.